PASJ: Publ. Astron. Soc. Japan **65**, 9, 2013 February 25

Spatially Resolved Near-Infrared Imaging of a Gravitationally Lensed Quasar, APM 08279+5255, with Adaptive Optics on the Subaru Telescope

Shin OYA,[1] Yosuke MINOWA,[1] Hiroshi TERADA,[1] Makoto WATANABE,[2] Masayuki HATTORI,[1] Yutaka HAYANO,[1] Yoshihiko SAITO,[3] Meguru ITO,[4] Tae-Soo PYO,[1] Hideki TAKAMI,[1,5] and Masanori IYE[5,6,7]

[1]*Subaru Telescope, 650 North A'ohoku Place, Hilo, HI 96720, USA*
oya@subaru.naoj.org
[2]*Department of Cosmosciences, Hokkaido University, Kita 10, Nishi 8, Kita-ku, Sapporo, Hokkaido 060-810*
[3]*Department of Physics, Tokyo Institute of Technology, 2-12-1 Ookayama, Meguro, Tokyo 152-8551*
[4]*Department of Electrical and Electronics Engineering, Kanazawa Technical College, 2-270 Hisayasu, Kanazawa, Ishikawa 921-8601*
[5]*National Astronomical Observatory of Japan, 2-21-1 Osawa, Mitaka, Tokyo 181-8588*
[6]*Department of Astronomy, The University of Tokyo, 7-3-1 Hongo, Bunkyo, Tokyo 113-0033*
[7]*Department of Astronomical Science, The Graduate University for Advanced Studies (SOKENDAI), 2-21-1 Osawa, Mitaka, Tokyo 181-8588*

(Received 2011 May 19; accepted 2012 August 30)

Abstract

We present a spatially resolved imaging analysis of a three-component gravitationally lensed quasar at $z = 3.91$, APM 08279+5255, in the L'- and M'-bands, and a narrow band centered at 3.05 μm using the 188-element adaptive optics system on the Subaru Telescope. The third, faintest quasar image, component C, has been clearly resolved in all of these bands for the first time. All of the three components are point sources in all three bands. No new component, neither a fourth quasar image nor a lens galaxy, was discovered. The observed bands correspond to the long-wavelength end of the optical power-law continuum of the source quasar in its rest frame, and are little contaminated by strong emission lines like Hα. The measured flux ratio of components C to B is shown to be constant in all of the observed bands, and its achromatic nature agrees well with preceding work done at short near-infrared wavelengths one decade ago. On the other hand, the flux ratio of components A to B shows an increase from that of past measurements. This could be ascribed to a microlensing event.

Key words: galaxies: quasars: individual (APM 08279+5255) — gravitational lensing — infrared: general — instrumentation: adaptive optics

1. Introduction

Gravitational-lens phenomena are useful astronomical tools for probing the properties of source quasars and lens galaxies at high redshift. APM 08279+5255 is one of the most famous gravitational-lens objects. The object was serendipitously discovered during a galactic carbon star survey, and its position coincided with an IRAS Faint Source Catalog source. Optical observations by Irwin et al. (1998) disclosed that the source is an extremely-luminous broad-absorption-line (BAL) quasar based on spectroscopy. The image showed an elongation under 0.″9 seeing, suggesting the possibility of gravitational lensing. Ledoux et al. (1998) confirmed gravitational lensing both spatially and spectroscopically, though the object was believed a double at that time. The accurate redshift, $z = 3.911$, of the source quasar was determined by radio observations of the CO emission line (Downes et al. 1999). The object has been a target of various observations over a wide range of wavelengths because of a variety of features besides gravitational lensing. For example, the properties of the absorbing gas causing X-ray BAL were discussed in Chartas et al. (2002). The Na I D absorption line of the damped Lyα system was first detected in the near-infrared spectrum by Kondo et al. (2006). The mass of the hot ($\sim$ 1300 K) dust was estimated by mid-infrared observation in Oyabu et al. (2009) and the extent of the warm ($\sim$ 200 K) dust region was determined by submillimeter observation in Krips et al. (2007). Riechers et al. (2009) showed the compactness of the lensed image of the molecular gas in the host galaxy by radio observations.

However, spatially resolved detailed studies from ground-based telescopes have been limited by a veil of atmospheric blur. The separation between the two main components, A and B, is only 0.″38, which is about half of the moderate seeing size at Mauna Kea. The third component, C, was found by two observations: Ibata et al. (1999) using HST NICMOS with the *F110W*, *F160W*, and *F205W* filters (centered at 1.1220 μm, 1.6028 μm, and 2.0658 μm, respectively) and Egami et al. (2000) obtaining K-band images with NIRC on the Keck I Telescope under exceedingly good seeing conditions (0.″15 in the K-band). Component C is slightly offset from the line connecting the brightest north-east component A and the south-west component B, with a separation of only 0.″14 from component A. The spatially resolved optical spectroscopy by Lewis et al. (2002) using STIS on HST confirmed that the third component is not a lensing galaxy, but an image of the source quasar. The flux ratios among the three components are known to show smooth and monotonic variation with the wavelength at optical and short near-infrared wavelengths.

However, decomposed properties of each component at long near-infrared wavelengths have not yet been observed. Currently, an adaptive optics system on an 8 m-class telescope is the only instrument capable of resolving component C under moderate seeing conditions at these wavelengths.

In this paper, we report on the first spatially resolved images at longer near-infrared wavelengths than preceding works, to extend the wavelength range for discussions on the nature of the gravitational lens object. The observations were realized by the 188-element adaptive optics system (AO188) on the Subaru Telescope. Throughout this paper, magnitudes are in the Vega system, and we assume cosmological constants of $h = 0.7$, $\Omega_{\rm m} = 0.27$, and $\Omega_\Lambda = 0.73$.

2. Observation and Data Reduction

Observations were made on 2009 December 11 (UT) with the 8-m Subaru Telescope (Iye et al. 2004) by using the AO188 adaptive optics system in the natural-guide-star mode (Hayano et al. 2008; Minowa et al. 2010). The object, itself (all of the components), was used as a natural guide star. The sky condition was photometric, and the seeing was 0.″7 in the K-band. AO188 is a curvature-sensing type adaptive optics system with 188 control elements (Takami et al. 2006). An automatic tip/tilt offload function from AO188 to the telescope secondary mirror was implemented recently (Oya et al. 2010), and used during observations. This function reduced the influence of the thermal background patterns caused by warm optics in AO188 at infrared wavelengths longer than 3 μm, and improved the detectability of the object.

All of the AO corrected images were obtained by IRCS (the InfraRed Camera and Spectrograph: Kobayashi et al. 2000), in the L'- and M'-bands and a narrow-band filter (centered at 3.050 μm with 0.152 μm FWHM). An ALADDIN III 1024 $\times$ 1024 InSb array was used in the camera side of IRCS. A pixel scale of $0.''02057 \pm 0.''00004\,{\rm pix}^{-1}$ was selected for all bands to make the best use of the high spatial resolution provided by AO. The images in each band were obtained in a 9-point dithering-pattern sequence, which consisted of a 3 $\times$ 3 grid with 2.″5 intervals. The image size was 1024 $\times$ 1024 pixels in the L'-band and the 3.05 μm filter, while being reduced to 512 $\times$ 512 pixels in the M'-band for fast readout. The exposure time and the number of obtained frames were 24 s and 27 frames (total 648 s) in the L'-band; 40 s and 63 frames (total 2520 s) in the M'-band; 30 s and 18 frames (total 540 s) in the 3.05 μm filter. HD 84800 was used as a standard star both for the L'-band, 7.547 ± 0.013 mag, and the M'-band, 7.56 ± 0.02 mag, taken from the UKIRT standard catalog (Leggett et al. 2003). Both the object and the standard were observed at airmasses of less than 1.27, and with airmass differences less than 0.08. No photometric standard star was observed for the 3.05 μm filter; hence, the data were used only to determine the relative position and flux ratio of the components.

A standard data-reduction process was applied using IRAF[1] software packages. First, we sky and dark subtracted in each frame using the average of the immediately before-and-after frames, as in Fadely and Keeton (2011). The difference of the sensitivity between pixels in each frame was corrected by dividing by a sky-based flat. The differences of the flat between the object and the standard are 5% for the L'-band and 10% for the M'-band. Because of the object size being less than 20 pixels, the difference of the flat within the extent was less than 0.5%. Next, each image was shifted to the center of the dithering pattern. The position of each image was determined with the 'imexam' command in IRAF, and aligned with a 0.1 pixel resolution to the peak of component B, except in the M'-band frames. The resolution was determined based on the repeatability. In the M'-band, the position of component A was used instead of B, because component B was too faint to determine an accurate peak position, and component C was faint enough not to affect the fitting. Then, all the images were combined by averaging.

The reduced images are shown in figure 1. The upper, middle, and lower panels in the figure correspond to the 3.05 μm filter, L'-band, and M'-band, respectively. The field-of-view of each panel is 1.″0 $\times$ 1.″0 (north is up, east is left). The left panels show the images reduced as described above. In all of these bands, the peak of component C is clearly separated from the others. The photometry for all three components together is presented in table 1. The fluxes were measured with the 1.″2 aperture diameter centered at the midpoint of components A and B. The 3.05 μm filter is not included in this table, because no photometric standard star was observed in this filter.

2.1. *Decomposition of the Three Components*

Since all of the three components are in close proximity, point-spread-function (PSF) decomposition is required to determine the relative positions and the flux ratios among the three components accurately. A caveat is that AO corrected PSFs are not necessarily axially symmetric and time-invariant. The PSF depends on the wavelength, and varies with time depending on the seeing conditions. Hence, it is difficult to express the PSF using a simple analytic profile. However, thanks to the small separation of the three components well within the isoplanatic angle, we can safely assume that the PSF is identical for all three components.

For the decomposition, the PSF was derived from the observed image by iteration, assuming that components A and B are essentially point sources. Iteration was necessary to reduce contamination from other surrounding peaks into the skirt of the PSF. A key point was to switch between the peaks of A and B in order to estimate the PSF from one step to the next, except just after the initial subtraction by an analytic profile. At each step, the PSF of either A or B estimated one step before was used to subtract surrounding features of the peak. Then, the remaining peak profile of the other component was used as the better estimated PSF for the next step. An advantage of the iteration method is that the final result does not depend on the initial analytic profile. Below we describe our procedure and several tests that we conducted to test the robustness of our procedure in detail.

First, initial subtraction was done by using a Moffat profile whose parameters were determined by radial profile fitting

[1] IRAF is distributed by the National Optical Astronomy Observatories, which are operated by the Association of Universities for Research in Astronomy, Inc., under cooperative agreement with the National Science Foundation.

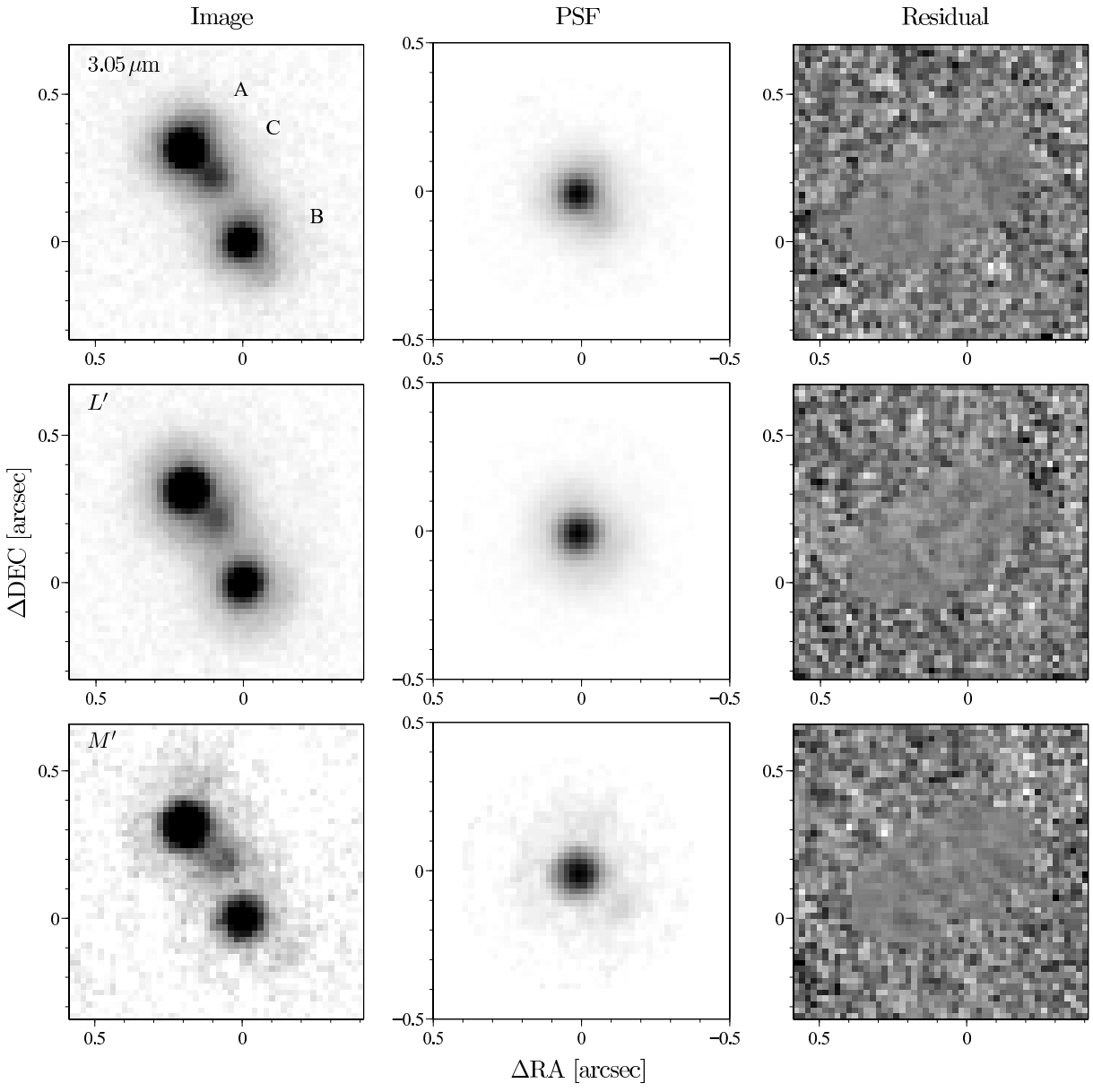

Fig. 1. Top, middle, and bottom panels are images for the 3.05 μm filter, L'-band, and M'-band filters, respectively. The size of each panel is $1''.0 \times 1''.0$ (north is up, east is left). The left panels are the observed images. To show the C component clearly, the images are linearly scaled with the half of the maximum of component A as black and the zero level as white. The center panels are the PSFs linearly scaled as black at the peak and white at the zero level. The right panels are linearly gray-scaled images of the residuals between $\pm 3\,\sigma$ of the sky level. The artificial blurry pattern around the center is the result of overlapping subpixel-shifted PSFs during subtraction and does not affect for analysis. The origin of the coordinates is at the peak of component B in the left and right panels.

Table 1. Photometry for the all three components together.

Band	Magnitude	F_ν [mJy]
L'	11.04 ± 0.14	9.5
M'	10.92 ± 0.30	7.2

using the 'imexam' command in IRAF. The PSF radius was set to 20 pixels ($0''.4$). Although 10% or less of the total flux might leak outside the radius, the influence to the relative position and the flux was negligible. Components A and C were subtracted from the original image to make the initial PSF from component B. After the initial subtraction, concentric negative and positive residuals were left around the first dark and bright diffraction rings of component A. At this point, the peak-to-valley values of the residuals were more than $10\,\sigma$ for the 3.05 μm filter and L'-band with high signal-to-noise ratio (S/N), and $6\,\sigma$ even for the M'-band with low S/N. A circular mask centered at the peak of A with a radius of 10 pixel ($0''.2$) was applied to eliminate the residuals for further iteration. The sky annulus was set between 25 and 30 pixels for the PSF fitting. The iteration was done using the DAOPHOT package in IRAF as follows. By using the initial PSF,

Table 2. Position and the flux of Components A and C relative to component B.

Band	A			C		
	ΔRA	ΔDec	Flux ratio	ΔRA	ΔDec	Flux ratio
3.05 μm	$0\farcs197 \pm 0\farcs002$	$0\farcs326 \pm 0\farcs002$	1.38 ± 0.01	$0\farcs086 \pm 0\farcs005$	$0\farcs213 \pm 0\farcs003$	0.22 ± 0.01
L'	$0\farcs198 \pm 0\farcs002$	$0\farcs326 \pm 0\farcs002$	1.39 ± 0.02	$0\farcs090 \pm 0\farcs002$	$0\farcs216 \pm 0\farcs002$	0.22 ± 0.01
M'	$0\farcs198 \pm 0\farcs002$	$0\farcs326 \pm 0\farcs002$	1.46 ± 0.05	$0\farcs099 \pm 0\farcs015$	$0\farcs215 \pm 0\farcs004$	0.21 ± 0.04

components A and C were first subtracted to produce the PSF of component B (B-PSF). The next step was to subtract components B and C using the B-PSF to make the PSF of component A (A-PSF). The final PSF of the band was generated by the average of the A-PSF and the B-PSF weighted by S/N. The difference of the average PSF from the A-PSF or the B-PSF is less than 0.9%, 0.7%, and 3% of the peak height over the entire profile for the 3.05 μm filter, L'-band, and M'-band, respectively.

The final synthetic PSF is shown in the middle panels of figure 1, and the residual of the fitting in the right panels. Note that there is no concentric residual left. The FWHM of the synthetic PSF is $0\farcs13$ in the 3.05 μm filter and L'-band; $0\farcs14$ in the M'-band. Even with poor seeing ($0\farcs7$ in the K-band), the AO corrected image size is slightly better than that obtained by Egami et al. (2000) in the K-band with extremely good seeing ($0\farcs15$ in the K-band). The position and the flux of components A and C relative to B were evaluated, as in table 2. To estimate the fitting error, the same analysis procedure was repeated with five artificial images generated by combining the model frame obtained by the fitting and a random noise frame. The error in table 2 refers to the standard deviation of the PSF fitting results for the five artificial images in each band.

The validity of the error range was also checked by applying the same fitting process to the following test cases. The results for all of the tests are consistent within the error. (1) A different analytic profile for the initial subtraction: Moffat profiles automatically determined by GALFIT (Peng et al. 2010) was used, as the initial analytic PSF. The β was fixed at 2.0 during the automatic fitting to prevent any divergence. The difference in the resulting FWHM from that used during the above analysis was 20%, at maximum. The initial residual was slightly improved. This test confirms that the results do not depend on the initial analytic PSF. (2) Difference by frame combination: the observed frames were divided into three sets, depending on the object position in the frame. Because the dithering pattern was a square matrix of 9 points, the frames are categorized into 3 sets: upper, middle, bottom rows. Each set was analyzed independently. This test indicates that the results are free of systematic error by local characteristics of the detector. (3) An influence of the seeing-halo or local background pattern: the leak of the flux from the center core spreads out to the size of seeing (called seeing halo). An extended Gaussian profile with the FWHM of the seeing size was subtracted from the observed image. The flux of the Gaussian profile was set to 10% of the total flux of all components (the estimated amount of the leak outside the PSF radius). This test shows that the results of the relative measurement are little affected by the small amount of flux left in the seeing halo, or any other local background pattern. (4) The detection of a 3σ offset: each parameter, the position (*RA*, *Dec*) and the flux in the model frame of the components A, B, C, was changed by 3σ to confirm that the offset could be correctly detected by the fitting procedure. The offset was applied one-by-one to each parameter of each component. The direction of the offset was selected toward more difficult fitting than the original condition, i.e., closer to the nearest component in the case of the position, fainter in the case of flux. Thus, the iteration method has a sensitivity equivalent to the error range.

3. Results

The object, APM 08279+5255, is clearly decomposed into three point sources in the L'- and M'-bands and in the 3.05 μm filter images (the corresponding rest wavelength at the source quasar is from 0.61 μm to 0.97 μm). This wavelength range corresponds to the long-wavelength end of the optical power-law continuum in its rest-frame, just before a steep rise of the thermal emission from dust (see, figure 1 in Oyabu et al. 2009). The observed bands are little affected by emission lines. The contamination of the blue wing of the Hα emission line into the 3.05 μm filter is less than 10%, based on NIR grism data from Oyabu et al. (2009). The L'- and M'-bands are free of major emission lines. No feature of elongation nor new component is found with a resolution of $\lesssim 0\farcs15$ within $3\farcs8 \times 3\farcs8$ around the object, though the observations were not intended to be deep. The 5σ limiting magnitude for a point source was 17.0 mag in the L'-band and 15.3 mag in the M'-band; for an extended object, the limiting magnitudes were 11.0 mag arcsec^{-2} in the L'-band and 10.8 mag arcsec^{-2} in the M'-band.

The relative positions of the three components in all of the observed bands are identical within the error (table 2). The separation between components A and B ($\theta_{\rm AB}$), and the separation between components C and B ($\theta_{\rm CB}$) were compared with those obtained by the past two observations (Ibata et al. 1999 in *F110W*, *F160W*, and *F205W* with HST and Egami et al. 2000 in the K-band with Keck I Telescope). Because no significant differences were found, the relative positions were averaged over all bands in the same observation (L'- and M'-bands and the 3.05 μm filter in this paper; *F110W*, *F160W*, and *F205W* in Ibata et al. 1999) for comparison. Our results differ from that of Ibata et al. (1999) by $0\farcs004$ for $\theta_{\rm AB}$ and by $0\farcs001$ for $\theta_{\rm CB}$, and from Egami et al. (2000) by $0\farcs001$ for $\theta_{\rm AB}$ and by $0\farcs012$ for $\theta_{\rm CB}$. All of these results, including ours, agree well, taking into account possible systematic errors associated among different instruments and/or analysis procedures.

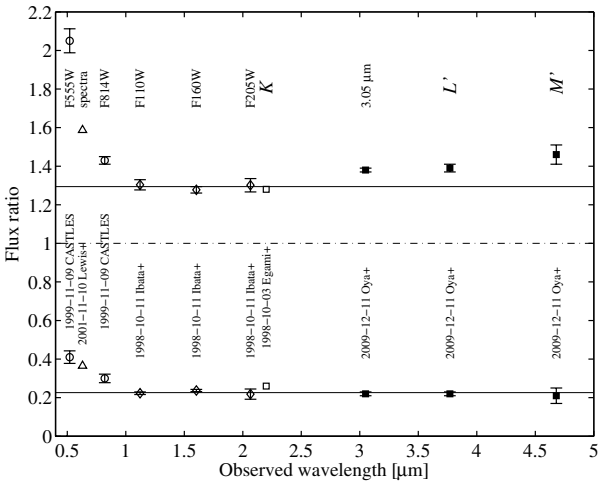

Fig. 2. Flux ratio of component A (upper) and component C (lower) to component B. The thin horizontal dash-dot line indicates a unity ratio level. The open circles are taken from CASTLES (HST, WF/PC2); the open triangles are from Lewis et al. (2002) (HST, STIS); the open diamonds are from Ibata et al. (1999) (HST, NICMOS); the open squares are from Egami et al. (2000) (Keck, NIRC); the filled squares are the results in this paper. The solid lines indicate the average of the HST NICMOS data for each ratio.

The obtained flux ratio of components A to B (A/B), and that of components C to B (C/B) are plotted in figure 2, together with data obtained from past observations (CASTLES;[2] Lewis et al. 2002; Ibata et al. 1999; Egami et al. 2000). The average value 0.23 ± 0.02 of C/B over all of the bands in our data is consistent with that of Ibata et al. (1999) observed about one decade ago. However, the average value, 1.41 ± 0.03, of A/B for all of the bands in our data is somewhat higher than those previously reported: 1.29 ± 0.03 by Ibata et al. (1999) and 1.28 by Egami et al. (2000). The result suggests a possible increase of the flux ratio, A/B, by 0.09 ± 0.03 mag due to variations along the time and/or wavelength.

4. Discussion

The wavelength range of spatially resolved observations of APM 08279+5255 was extended by our work up to 4.7 μm by using the Subaru adaptive optics system. At wavelengths shorter than 2 μm, the spatially resolved flux ratios among the three components observed by HST have been available over a wide wavelength range: optical (*F555W* and *F814W*, centered at 0.52 μm and 0.82 μm, respectively) in the CASTLES data base; continuum (6250 Å–6350 Å) in Lewis et al. (2002); near-infrared (*F110W*, *F160W*, and *F205W*) in Ibata et al. (1999). Egami et al. (2000) also presented data observed in the *K*-band by the Keck I Telescope under excellent seeing conditions. Note that the data at wavelengths shorter than 2.0 μm were obtained within a two-year time-span one decade ago,[3] as indicated in figure 2. At short near-infrared wavelengths (1.2 μm–2.2 μm), the flux ratios are almost constant and independent of the wavelength. On the other hand, in the optical band, both flux ratios A/B and C/B increase smoothly, but steeply toward shorter wavelengths. Yonehara et al. (2008) discussed the possibility of both differential extinction and a microlensing event to explain the smooth and monotonic wavelength variation of the flux ratio, A/B, in HST data between 0.5 μm and 2.0 μm. Although the color difference of the object is slightly outside the range predicted by the typical parameters assumed in Yonehara et al. (2008), they mentioned a flatter extinction law (in the differential extinction case), or larger scale length of caustics (in the microlensing case) as possible explanations for the color.

Our data reveal some new behavior of the flux ratio at longer wavelengths, and after a long time-interval. The independence of the flux ratios from wavelengths greater than 1 μm is the same as the result by Ibata et al. (1999), even at the extended wavelength range of our observations from 3.1 μm to 4.7 μm. However, the flux ratio A/B increases slightly (0.09 mag) from past observations at shorter wavelengths ten years ago, while the flux ratio C/B does not change. There are several possible explanations for the observed changes in the flux ratio: microlensing, differential extinction, and differential time-delay. We discuss each of these possibilities in detail below. Of these, the microlensing scenario provides a better explanation of our results than the other two.

4.1. *Microlensing*

One possibility for interpreting the observed feature is a time-variation caused by microlensing (e.g., Kayser et al. 1986). A stellar-mass object is able to magnify the flux when the object passes in front of one of the components. A flux variability of 1 mag or more is not unusual. For example, Q 2237+0305 is a famous object for such a microlensing phenomenon (e.g., Woźniak et al. 2000; Alcalde et al. 2002). For APM 08279+5255, an almost achromatic increase of the flux ratio A/B by 0.09 mag was found from short near-infrared wavelengths (1.2 μm–2.2 μm: Ibata et al. 1999; Egami et al. 2000) to our long near-infrared measurement (3.1 μm–4.7 μm). It is natural to attribute the increase of the flux ratio A/B in our result from the past two results to the time-variation over one decade. The slow rate of the time-variation (~ 0.1 mag decade^{-1}, unless we missed the highest peak of the variation during the past decade), is consistent with the time scale expected toward this object in the case of microlensing (e.g., 30 to 100 yr[4] as in Oyabu et al. 2009). If a microlens event increased the flux ratio A/B, component A seems to be magnified, because the flux ratio C/B has not changed. Lewis et al. (2002) also suggested the possibility of microlensing toward this object based on spatially resolved spectroscopic observations. They pointed out that the flux ratios of the continuum are different from that of a broad emission

[2] CfA-Arizona Space Telescope LEns Survey at ⟨http://www.cfa.harvard.edu/castles/⟩.

[3] The dates of HST optical observations were identified from the archive utilizing MAST at ⟨http://archive.stsci.edu/⟩.

[4] The time scale is Einstein time. The source crossing time is expected to be almost same (or even larger depending on the magnification by the lens) because of large luminosity of the object, according to equations (3) and (4) in Chiba et al. (2005).

line among the three components of APM 08279+5255. Because a magnification by the microlens varies with the source size, such a difference is explained if the size of the emitting region changes between the continuum and the emission lines, as generally expected for quasars. Interestingly, the flux ratio of the continuum and that of the emission line does not match for any pair of the three components. This would mean that at least two of three components are affected by microlensing. They mentioned that component B appeared to be magnified, and C appeared to be demagnified compared to A. It would be difficult to conclude which is the non-microlensed steady component without long-term monitoring based on the same observation and analysis method.

A similar flux anomaly among components could also be caused by substructures of the lensing galaxy (e.g., Kochanek & Dalal 2004). The phenomenon is called millilensing (e.g., Fadely & Keeton 2011) because its effect is on a milliarcsecond scale. A typical timescale of the effect is long (~ 1000 yr), and magnification by the effect is expected to be less susceptible to the size of the continuum emitting region of the source quasar. A speculation is that a part of the complicated flux anomaly of the object can be attributed to millilensing. Determining the microlensing and/or millilensing effect is important for discussions on the lens model. For example, Riechers et al. (2009) proposed a new lens model, in which the constraints on the flux ratio were relaxed, taking into account a possible change in the flux ratio by microlensing. Because the flux ratio observed at near-infrared wavelengths is rather independent of the wavelength, compared with that observed at optical wavelengths, simultaneous spatially resolved observations in all of the near-infrared bands would be conclusive for distinguishing the time variation from static chromatic variations, though it would take a long time to detect the time variation ($\gtrsim 1$ yr even in the case of microlensing).

4.2. *Differential Extinction*

Because light from each component of a gravitational lens system passes a different position of the lensing galaxy, the flux ratios among components are susceptible to local extinction in the galaxy. Differential extinction by a lensing galaxy is a common phenomenon observed among gravitationally lensed systems. For example, according to Falco et al. (1999), only one third of their lensed-quasar sample is free of differential extinction. Lewis et al. (2002) pointed out the possible influence of differential extinction, especially for component C. This is supported by a lens-model of an edge-on spiral lens-galaxy proposed by Riechers et al. (2009), which reproduces the compactness at radio wavelengths. Our results show that it is difficult to explain all of the observed flux-ratio variation along wavelength by the differential extinction alone, because the change in the flux ratio of A/B is not monotonic. Figure 2 also indicates that, if the increase of the flux ratios at optical wavelengths is attributed to the differential reddening among the components, the most reddened component would be B.

4.3. *Differential Time-Delay of Intrinsic Variability*

The optical path length is different for each component of a gravitational-lens system. Thus, the same event at the quasar is observed with different time-delays among the components, which causes an apparent flux ratio difference at the time of observation. Although the time variation of the total flux toward APM 08279+5255 is reported in the R-band as 0.2 mag for 100 days in Lewis, Robb, and Ibata (1999), this intrinsic variability seems to be insufficient to change the flux ratio of the object. Because the separation of images is small, the time-delay among the components is expected to be short. However, since the observed increase amount of the flux ratio A/B (0.09 mag) is small, we estimate a differential time-delay of the intrinsic variability toward the object. First, the time-delay between A and B was estimated to be less than one day by equation (2) in Yonehara et al. (2008) for a lens redshift less than 3, referring to the three-image lens model in Egami et al. (2000). Next, the expected magnitude difference for the time-delay was calculated by equation (3) in Yonehara et al. (2008). According to the equation, the structure function of the intrinsic variability is in proportion to $(\Delta t/\lambda)^{0.3}$, where Δt is the time lag and λ is the wavelength. Here, we scaled the observed R-band variation (0.2 mag with $\Delta t = 100$ day and $\lambda = 0.66\,\mu$m)[5] to the time lag of 1 day by the lens and in the L'-band of our measurement ($\Delta t = 1$ d and $\lambda = 3.77\,\mu$m). The result of the calculation is 0.03 mag, still three-times smaller than the observed value of 0.09 mag.

5. Summary

We presented a spatially resolved imaging analysis of a gravitationally lensed object, APM 08279+5255, in the L'-band, and M'-band, and a narrow-band centered at 3.05 μm. A high spatial-resolution of better than $0\farcs14$ was achieved by the 188-element adaptive optics system on the Subaru Telescope even in a natural-guide-star mode. All of the three components (A, B, and C) were clearly resolved at wavelengths longer than 3 μm for the first time. No sign of elongation for any component was detected. Photometric measurements were obtained in the L'-, and M'-bands. The observed wavelength range corresponds to the long-wavelength end of the rest-frame optical power-law continuum of the source quasar. No new component was found within a $3\farcs8$ square region around the object. The relative positions of the components agree well with past observations. The flux ratio C/B is constant over a wide wavelength range (1.2 μm–4.7 μm), and remains unchanged for over one decade. On the other hand, the flux ratio A/B increases by 0.09 mag in our result. This variation is likely due to a slowly varying microlensing event of the lens, rather than to differential extinction by dust in the lens galaxy, or to a differential time-delay of intrinsic variability. A spatially resolved observation over time in the near-infrared bands will conclusively distinguish these possibilities.

We would like to thank all staff members of Subaru Telescope, and the National Astronomical Observatory, Japan, who kindly supported our research. Special thanks are due to Shinki Oyabu, who provided the table of data in figure 1 of their paper, and information on the time-delay. SO is grateful to Masatoshi Imanishi for discussions on AGN properties to estimate the time-delay. We acknowledge useful comments from

[5] Two times larger (or more depending on the magnification by the lens) than the expected value by the structure function.

an anonymous referee, who improved this paper. AO188 is a part of the Subaru laser-guide-star adaptive-optics project, which has been supported by a Grant-in-Aid for Specially Promoted Research (14002009) from the Japan Ministry of Education, Culture, Sports, Science and Technology and by the Grant-in-Aid for Scientific research [(S)19104004] from Japan Society for the Promotion of Science.

References

Alcalde, D., et al. 2002, ApJ, 572, 729
Chartas, G., Brandt, W. N., Gallagher, S. C., & Garmire, G. P. 2002, ApJ, 579, 169
Chiba, M., Minezaki, T., Kashikawa, N., Kataza, H., & Inoue, K. T. 2005, ApJ, 627, 53
Downes, D., Neri, R., Wiklind, T., Wilner, D. J., & Shaver, P. A. 1999, ApJ, 513, L1
Egami, E., Neugebauer, G., Soifer, B. T., Matthews, K., Ressler, M., Becklin, E. E., Murphy, T. W., Jr., & Dale, D. A. 2000, ApJ, 535, 561
Fadely, R., & Keeton, C. R. 2011, AJ, 141, 101
Falco, E. E., et al. 1999, ApJ, 523, 617
Hayano, Y., et al. 2008, Proc. SPIE, 7015, 701510
Ibata, R. A., Lewis, G. F., Irwin, M. J., Lehár, J., & Totten, E. J. 1999, AJ, 118, 1922
Irwin, M. J., Ibata, R. A., Lewis, G. F., & Totten, E. J. 1998, ApJ, 505, 529
Iye, M., et al. 2004, PASJ, 56, 381
Kayser, R., Refsdal, S., & Stabell, R. 1986, A&A, 166, 36
Kobayashi, N., et al. 2000, Proc. SPIE, 4008, 1056
Kochanek, C. S., & Dalal, N. 2004, ApJ, 610, 69
Kondo, S., et al. 2006, ApJ, 643, 667
Krips, M., Peck, A. B., Sakamoto, K., Petitpas, G. B., Wilner, D. J., Matsushita, S., & Iono, D. 2007, ApJ, 671, L5
Ledoux, C., Théodore, B., Petitjean, P., Bremer, M. N., Lewis, G. F., Ibata, R. A., Irwin, M. J., & Totten, E. J. 1998, A&A, 339, L77
Leggett, S. K., et al. 2003, MNRAS, 345, 144
Lewis, G. F., Ibata, R. A., Ellison, S. L., Aracil, B., Petitjean, P., Pettini, M., & Srianand, R. 2002, MNRAS, 334, L7
Lewis, G. F., Robb, R. M., & Ibata, R. A. 1999, PASP, 111, 1503
Minowa, Y., et al. 2010, Proc. SPIE, 7736, 77363N
Oya, S., et al. 2010, Proc. SPIE, 7736, 77363U
Oyabu, S., Kawara, K., Tsuzuki, Y., Matsuoka, Y., Sameshima, H., Asami, N., & Ohyama, Y. 2009, ApJ, 697, 452
Peng, C. Y., Ho, L. C., Impey, C. D., & Rix, H.-W. 2010, AJ, 139, 2097
Riechers, D. A., Walter, F., Carilli, C. L., & Lewis, G. F. 2009, ApJ, 690, 463
Takami, H., et al. 2006, Proc. SPIE, 6272, 62720C
Woźniak, P. R., Udalski, A., Szymański, M., Kubiak, M., Pietrzyńsky, G., Soszyński, I., & Żebruń, K. 2000, ApJ, 540, L65
Yonehara, A., Hirashita, H., & Richter, P. 2008, A&A, 478, 95